ENERGY DISSIPATION IN WEB-FLANGE JUNCTIONS OF PULTRUDED GFRP DECKS

Sonia Yanes[1], Julia de Castro[1] and Thomas Keller[1]

[1]Composite Construction Laboratory, École Polytechnique Fédérale de Lausanne
EPFL-ENAC-CCLAB, BP 2225, Station 16, CH-1015 Lausanne, Switzerland
Email: thomas.keller@epfl.ch, web page: http://cclab.epfl.ch

Keywords: Pultruded FRP bridge decks, Pseudo-ductility, Energy dissipation, Mechanical testing

ABSTRACT

The energy dissipation capacity resulting from progressive cracking of the web-flange junctions (WFJs) of a pultruded GFRP deck system was experimentally investigated. Web-cantilever bending experiments up to failure were performed on two WFJ types (*IfO*, *IcO*) with similar geometry and fiber architecture but different initial imperfections. The latter resulted in different load-displacement behaviors (linear and markedly nonlinear up to failure in *IfO* and *IcO*, respectively) and failure modes. Failure was governed in both types by through-thickness tension in the tensioned fillet. However, different crack sequences were observed due to the fiber architecture and resulted in an abrupt failure in *IfO* and a more progressive failure in *IcO*, in addition to a higher load-bearing capacity of the latter. The total and dissipated energies of the *IcO* WFJs and their ductility index, defined as the ratio of the dissipated to total energy, were modeled. The ductility index did not significantly increase as from a given displacement. The main energy dissipation mechanism of the *IcO* WFJs was related to crack development; dissipation through viscoelastic losses was significant only at low deflection levels.

1 INTRODUCTION

Glass fiber-reinforced polymer (GFRP) bridge decks constitute one of the most widely developed applications of FRP structural materials in the civil engineering field. Since the 1990s, GFRP bridge decks have been increasingly used in road and footbridges, both for new structures and the upgrading of existing ones, due to advantageous properties compared to decks composed of traditional materials.

Despite the good potential of FRP materials for structural applications, other features have delayed their more widespread use, including their lack of inherent ductility [1, 2]. Structural safety considerations require structures to be robust, i.e., to be capable of sustaining unforeseen loads to which they might reasonably be subjected [3]. Inherent material ductility represents a main advantage to provide robustness with which structural engineers are familiar. Ductile materials permit the redistribution of internal forces and dissipation of energy under impact and seismic actions. Material ductility also results in large structural deformations although without any decrease in load-bearing capacity prior to ultimate failure, therefore representing a warning of possible structural problems. Unexpected brittle failure is unacceptable in civil structures however, which consequently results in the large safety margins required in the design procedure.

FRPs typically used in civil engineering consist of non-ductile components. The material's brittle behavior results in reduced structural ductility and prevents an optimized use of their strength properties. Given the lack of ductility of FRP material constituents, alternative approaches have to be developed. Ductility can be provided on the material and/or the structural system level, referred to as material and system ductility respectively. Two different sub-concepts can be distinguished on each level: (i) ductility, referring to the combination of ductile and brittle constituents or components; (ii) pseudo-ductility, comprising only brittle constituents or components [1].

A primary strategy to provide material ductility is the incorporation of new ductile constituents (matrices and fibers). A nonlinear inelastic behavior, with decreasing stiffness at higher load levels, similar to ductile materials, can be attained through material hybridization, by using different fiber orientations and/or by employing alternative manufacturing techniques, e.g. braiding. Pseudo-ductility can be improved by controlling the damage mechanisms.

Reviews on the ductility and pseudo-ductility of FRP composites on the system level can be found in [1, 2]. System ductility can be achieved through the integration of ductile structural components or connections. In the absence of ductile components, system pseudo-ductility can be attained by progressive failure in the brittle components/connections providing that structural redundancy in the system (static indeterminacy), in the cross section and/or at the component level exists. The structural system redundancy provides alternative load paths and force redistribution as local failures occur in the components or in the connections. Nonetheless, pseudo-ductile structures become statically determinate after a certain number of internal failures and a further failure would result in abrupt collapse. At the cross-sectional level, redundancy can be provided in multi-component cross sections, using one or several materials. Failure of the first material/component or connection between the components does not necessarily lead to failure of the whole section, and internal force redistribution functions as in statically indeterminate systems. Nonlinear, inelastic behavior providing pseudo-ductility by means of progressive internal failures can also be found at the component level [4]. Other approaches to obtain gradual and controlled failure in FRP structural components, allowing the development of a nonlinear, inelastic increase in deformation and leading to the dissipation of internal strain energy, consist of a design for non-catastrophic failure modes, e.g. tearing failure at the junctions in pultruded members. The tensile tearing failure mode, leading to flange separation, has been observed after buckling of the flange(s) and/or web of pultruded I-profiles subjected to bending or axial compression and has been found to result in a nonlinear pseudo-ductile load-deflection behavior for entire frame structures.

In a previous investigation [5], the load transfer mechanism and failure mode, in the transverse-to-pultrusion direction, of a GFRP deck system (*DS*) with trapezoidal cell cross section subjected to three-point bending were experimentally studied. The deck exhibited a frame-dominated behavior whereby the load was mainly transmitted by local shear and bending moments in the web and flange elements (Vierendeel frame mechanism). Gradual cracking in the web-flange junctions (WFJs) was detected and led to a stiffness reduction without causing the deck's final failure. A non-brittle failure was observed and sustained load-bearing capacity under the development of large displacements was registered. This was attributed to the system redundancy – progressive local bending failures occurred in the WFJs. The unloading cycles performed after the initiation of damage in the WFJs and prior to final failure demonstrated that the deck was able to dissipate internal energy through the inelastic increase in deformation caused by the internal local failures.

The objective of this work is the experimental investigation of the energy dissipation capacity resulting from progressive cracking of the WFJs of the *DS* deck. Two types of WFJs with similar geometry but different locations within the deck profile were investigated. A visual examination of the deck had revealed that, despite the similar geometry of the two WFJ types, slight dissimilarities in the fiber architecture and different initial imperfections existed. Their influence on the WFJs' behavior was studied. Given the viscoelastic character of FRP materials – FRPs may exhibit viscoelastic behavior because of the polymeric nature of their matrix – the sensitivity of the response to different loading/unloading rates was also assessed. Web-cantilever bending experiments up to failure were performed on 50-mm-wide specimens. The response of both series is compared and discussed. The energy dissipation capacity of the WFJs under monotonic loading was evaluated using existing ductility indices.

2 THEORETICAL BACKGROUND

2.1 Energy dissipation in viscoelastic materials

Viscoelastic materials are able to both store and dissipate energy under load owing to their viscous properties, in contrast to ideal Hookean elastic solids, which are capable of energy storage but not energy dissipation. During the deformation of an ideal viscoelastic material with no residual deformation (see Fig. 1 (a)), the total energy supplied during loading through the work of the external loads, W_t, can be formulated as:

$$W_t = W_e + W_{d,hyst} \tag{1}$$

where W_e = elastic energy, i.e. energy elastically stored during loading and released upon instantaneous unloading; $W_{d,hyst}$ = energy dissipated through viscosity-related friction losses, also referred to as hysteretic energy [6]. The elastic energy is represented by the area below the unloading path and the hysteretic energy is related to the area within the hysteretic loop, see Fig. 1 (a).

In viscoelastic materials subjected to plasticity or damage, besides $W_{d,hyst}$, part of the total energy is dissipated through plasticity and damage mechanisms, $W_{d,dam}$, leading to a non-recoverable, permanent deformation δ_{res} (see Fig. 1 (b)). The total energy provided to the system can be expressed as:

$$W_t = W_e + W_{d,hyst} + W_{d,dam} \tag{2}$$

where the addition of $W_{d,hyst}$ and $W_{d,dam}$ represents the total dissipated energy, W_d.

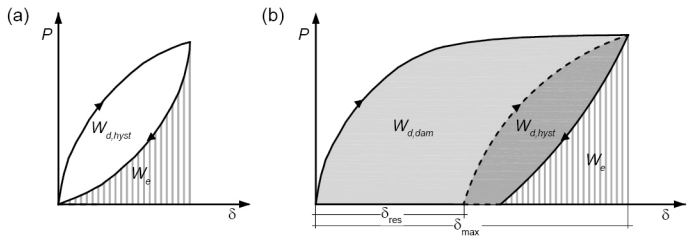

Figure 1: Energy dissipation in (a) viscoelastic materials with no residual deformation; (b) viscoelastic materials with residual deformation under monotonic loading.

2.2 Ductility evaluation

Ductile structural materials, elements or systems are characterized by their ability to sustain inelastic deformation without loss of their load-bearing capacity and dissipate energy during impact and reverse cyclic loading. Ductility can be expressed, following this definition, in terms of energy dissipation. A large energy dissipation capacity can be considered as a ductility indicator. The ratio of the energy dissipated at failure, W_d, to the total energy supplied by the work of the external loads, W_t, has been proposed as a ductility index μ [7]:

$$\mu = \frac{W_d}{W_t} \tag{3}$$

For viscoelastic materials showing residual deformation, Eq. (3) can be formulated as:

$$\mu = \frac{W_{d,hyst} + W_{d,dam}}{W_t} \tag{4}$$

3 EXPERIMENTAL PROGRAM

The investigation is based on small-scale experiments conducted on the web-flange junctions (WFJs) of the DuraSpan (*DS*) pultruded GFRP bridge deck system.

3.1 Pultruded GFRP bridge deck system

The cross section of the *DS* unit module profile consists of two trapezoidal cells shaped by vertical and slightly inclined webs connected to the deck's face sheets (flanges). The dual-cell unit profiles are bonded together along their vertical (outer) webs using a structural polyurethane adhesive to form the slab, see Fig. 2 (a). A tongue-and-groove connection between adjacent profiles is provided by lip extensions and steps in the deck's face sheets, on opposite sides of the unit profile. The *DS* deck is composed of E-glass fibers embedded in an isophthalic polyester resin. The fiber stacking sequence of the laminates alternates roving in the pultrusion direction, triaxial multi-ply fabrics and additional non-structural mats.

3.2 Specimen description and preparation

The *DS* deck's WFJs can be classified into two groups according to the corresponding web geometry: vertical (*V*) and inclined (*I*). Two *I* WFJ types can be differentiated depending on the closer (*c*) / farther (*f*) location of the adhesively-bonded profile-to-profile joint in the flange in regard to the WFJ itself. Within the framework of this study, the *Ic* and *If* WFJ types were investigated under local bending moment, in relation to the frame-dominated behavior exhibited by the *DS* deck in its transverse-to-pultrusion direction [5].

The experimental program was conducted on three *If* and five *Ic* specimens. The specimens were labeled *IfO-m* (m = 1–3) and *IcO-n* (n = 4–6 and 8–9). The third character (*O*) of the specimens' appellation denotes the direction of the local bending moment in the web element – *O* indicates the tensioned side of the web towards the obtuse angle of the WFJ (see Fig. 2 (b)). The specimens' location within the deck panel and their overall geometry are shown in Fig. 2. The average width, b, and thickness, t_w, of the specimens' webs were 49.2±0.7 and 11.4±0.1, respectively.

The typical fiber architecture of both WFJs examined is schematically illustrated in Fig. 3. Two thirds of the triaxial multi-ply fabrics from the web laminate are prolonged into the flange. As a result, the flange thickness is greater close to the WFJ. At the center of the WFJ there is an approximately triangular-shaped roving core. A visual examination of the specimens was conducted and showed that, due to initial imperfections, differences existed between their actual fiber arrangement and the fiber architecture design, see Fig. 4. In the *IfO* specimens, these imperfections consisted of: (i) a resin pocket in the WFJ, towards the WFJ's acute angle and (ii) the uneven distribution of the triaxial fabrics, concentrated towards the acute angle side, across the web thickness, see Fig. 4 (a). In the *IcO* series, the observed flaws comprised: (i) the prolongation of the continuous web-flange triaxial fabrics into the small-thickness region of the flange and (ii) the wrinkling of the innermost fabric (obtuse angle side) in the radius area, see Fig. 4 (b). Furthermore, during the visual inspection, a small crack (referred as "pre-crack" in the following) of 20–40-mm length was observed in the flange of every *IcO* specimen, see also Fig. 3 (b). The pre-crack was located towards the obtuse angle side of the WFJ and ran parallel to the flange element at a ca. 8-mm depth from the laminate's surface.

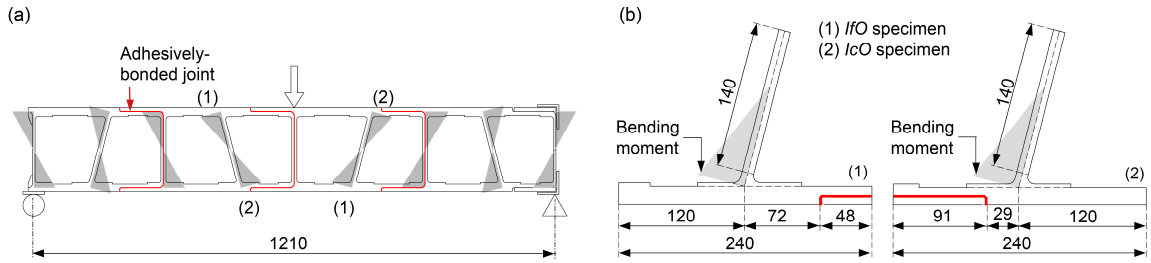

Figure 2: (a) Local bending moments in webs of *DS* deck panel subjected to transverse bending. (b) WFJ specimens; dimensions in mm.

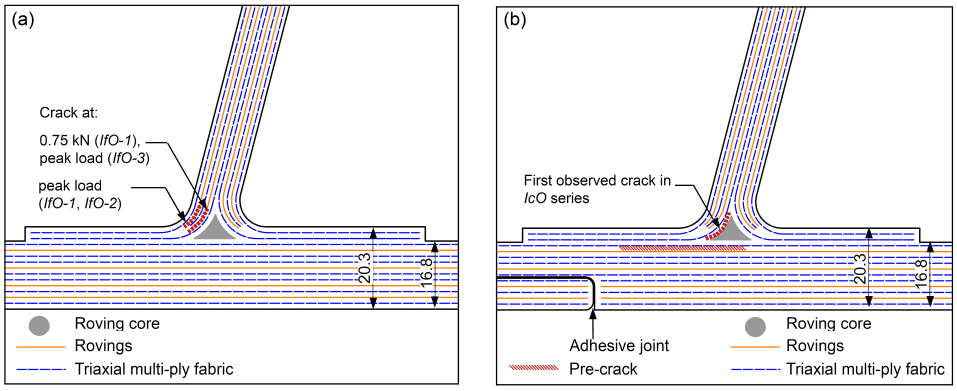

Figure 3: Fiber architecture and crack initiation of (a) *IfO* and (b) *IcO* series; dimensions in mm.

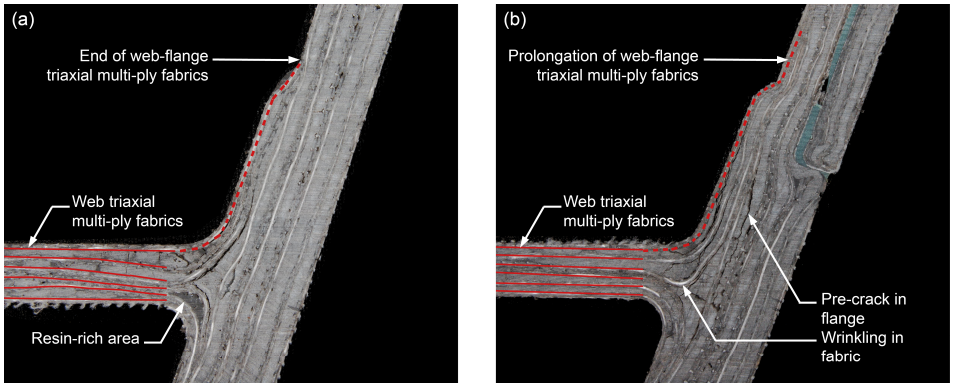

Figure 4: Initial imperfections of (a) *IfO* and (b) *IcO* series. Note: view of specimens after experiments; web triaxial multi-ply fabrics marked in red continue towards the flange.

3.3 Experimental set-up, instrumentation and procedure

The WFJ specimens were loaded under local bending applied to the web element. The specimens' webs were loaded as a cantilever with a 65-mm lever arm and clamped flange, see Fig. 5. A single support fixture allowing the conducting of the web-cantilever experiments on all WFJ types using a universal testing machine was designed and manufactured. The set-up is shown in Fig. 5. The web of the specimen was placed horizontally and the flange element was laterally clamped. The 20.3-mm-thickness flange area close to the WFJ (see Fig. 3) remained unclamped. Contact between the loading fixture and the upper face of the specimen's web was across the whole width of the web.

The rotations of the specimen's flange and web and the vertical deflections along the length of the latter were measured by means of a video extensometer throughout the experiments. The video extensometer system was also used to automatically capture and save images of the specimen at regular intervals during the experiments.

All experiments were conducted under displacement control up to failure. The *IfO* specimens were monotonically loaded at a rate of 0.01 mm/s. The *IcO* specimens were subjected to several unloading-reloading cycles delimited by previously defined maximum machine displacements, δ_{max}, ranging from 5 to 20 mm. The influence of the displacement rates during loading/unloading was investigated with regard to the potential viscoelastic behavior of the material. The displacement rates during loading/reloading, v_l, ranged from 0.01 to 0.10 mm/s and the rates during unloading, v_u, from 0.01 mm/s to 1.50 mm/s. After unloading, the load was sustained at 0.1 kN for a period of time ranging from 5 min to 60 min during which the deflection recovery was measured.

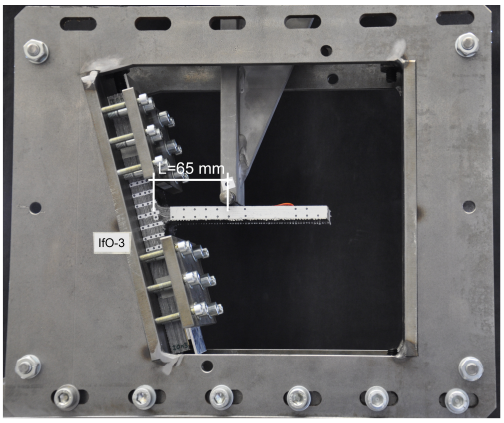

Figure 5: Experimental set-up.

4 EXPERIMENTAL RESULTS

4.1 *IfO* series response

The load-deflection (P-δ) responses registered for the *IfO* series are shown in Fig. 6 (a). A small rotation in the flange element, on its rear side, was registered. Its contribution to the total deflection was subtracted from the measured vertical deflections of the WFJ specimen's web under the load application point, in order to eliminate the effect of the unclamped flange area from the web's response.

All the *IfO* specimens showed similar initial stiffness, as indicated by coincident P-δ plots. Specimen *IfO-1* displayed a linear P-δ relationship up to a ca. 0.75-kN load, when the first crack was observed in the upper (tensioned) fillet of the WFJ, parallel to its surface. The first crack appeared adjacent to a triaxial fabric of the web without continuity into the flange, towards the inner part of the WFJ, see Figs. 3 (a) and 7 (a)). The stiffness decreased and the initially linear response became slightly nonlinear up to failure, which occurred suddenly at a 0.96-kN load when a second crack was observed, parallel to the first one and closer to the WFJ surface. It also occurred adjacent to the abovementioned fabric but towards the outer side of the WFJ (see Figs. 3 (a) and 7 (a)). Specimens *IfO-2* and *IfO-3* exhibited linear behavior up to failure, which occurred abruptly at 1.05- and 1.28-kN loads, respectively. At the peak load, a delamination crack was observed in a similar location to either the pre-failure or failure crack of *IfO-1*, see Figs. 3 (a) and 7 (a). No damage had been previously detected.

Failure was governed by transverse (through-thickness) tension in the fillet region of the WFJs under tension. The average ultimate load per unit width (P_{ult}/b) was 22.2±3.3 N/mm. Load decreases of 38±6% were registered after failure. Subsequently, specimens were able to bear an approximately constant (0.58–0.80-kN), slightly decreasing load under large displacement development, see Fig. 6 (a). As the displacement increased, other delamination cracks appeared and propagated near the continuous web-flange triaxial fabrics in the WFJs' tensioned side, as shown in Fig. 7 (a).

4.2 *IcO* series response

The load-deflection responses measured for the *IcO* series are shown in Fig. 6 (b). The deflection caused by the rotation of the flange was discounted as for the *IfO* series. The overall behavior of the five *IcO* specimens was analogous regardless of their different loading programs and displacement rates. All the specimens exhibited linear behavior up to a load of ca. 0.50–0.70 kN (proportional limit) in the first cycle. The propagation of the pre-existing crack in the specimens' flange (see Section 3.2) was then noticed. The behavior changed to nonlinear, with a marked reduction of stiffness and large displacement development towards failure. Progressive delamination cracks were observed in the upper (tensioned) fillet of the WFJs as from the proportional limit without producing the specimens' final failure. The appearance and propagation of cracking occurred with increasing displacement throughout the cycles. The first cracking – apart from the pre-crack in the flange – initiated between the triangular-shaped roving core, in the WFJs' tensioned side, and the adjacent triaxial web-flange fabric, as indicated in Figs. 3 (b) and 7 (b). Before the peak load was reached, other delamination cracks appeared in the tensioned fillet, adjacent to the triaxial fabric of the web without continuity into the flange, in the same locations as those observed in the *IfO* series at peak load (see Figs. 3 (a) and 7 (b)). Due to the progressive cracking, the specimens showed decreasing stiffness during reloading with increasing displacement at unloading. Reloading paths deviated from the unloading paths in the cycles conducted on all the specimens.

Failure, defined as the peak load, occurred at 1.20–1.50 kN in the *IcO* specimens, which corresponds to a 28.2±2.1-N/mm load per unit width. The corresponding displacement ranged from 14 to 20 mm. Noticeable load drops were afterwards observed under increasing displacement, see Fig. 6 (b). The *IcO* specimens failed due to the propagation of the previously formed delamination cracks (as from a 0.55-kN load in the first cycle) caused by transverse tension in the upper fillet of the WFJs. No differences were detected in the *IcO* specimens' failure modes irrespective of the dissimilarities in the experimental procedure.

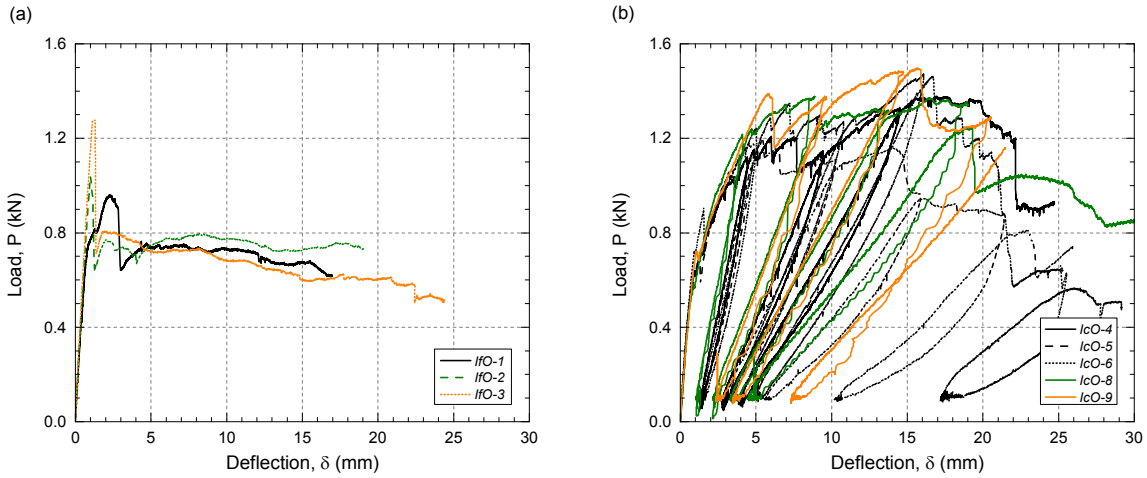

Figure 6: Load-displacement response of (a) *IfO* and (b) *IcO* specimens.

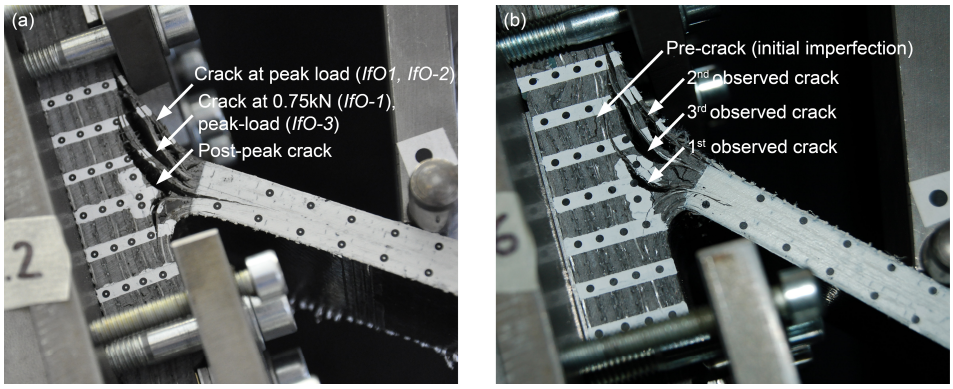

Figure 7: Post-peak crack pattern of (a) *IfO-2* and (b) *IcO-6* specimens.

5 DISCUSSION

5.1 Comparison of *IfO* and *IcO* series

The *IfO* and *IcO* specimens had similar geometry, which only differed in the location of the adhesively-bonded profile-to-profile joint in the flange element in respect to the WFJ itself. Furthermore, their fiber architecture design was equal, although visual inspection of the specimens had revealed that differences existed between the two series due to initial imperfections. The different load-displacement behavior, failure mode and strength registered for the two series are now discussed and compared with regard to the aforesaid dissimilarities.

The *IfO-1* / *2* / *3* specimens exhibited linear behavior up to 78 / 100 / 100% of their peak load. The *IcO* specimens displayed nonlinear behavior with the proportional limit at ca. 35–50% of their peak load. The average tangent initial stiffness of the *IfO* and *IcO* specimens, defined as the load per unit width to be applied to produce a unit vertical displacement under the load application point, was 26.1±1.4 and 20.2±1.9 N/mm mm respectively, which represents a ca. 25% difference. This difference increased as from the proportional limit of the *IcO* specimens due to their significant reduction in stiffness. The difference of rotation ($\Delta\theta_{web}$) between two sections of the specimens' webs located at 25 and 65 mm from the WFJ were measured during the first loading cycle, which exceeded the proportional limit of the *IcO* series. Linear relationships with load were registered in both series, with a 13% difference between them. This showed that the web element remained undamaged and that the stiffness decrease in the *IcO* specimens was not related to the web – its fiber stacking sequence was equal in the *IfO* and *IcO* specimens, see Fig. 3.

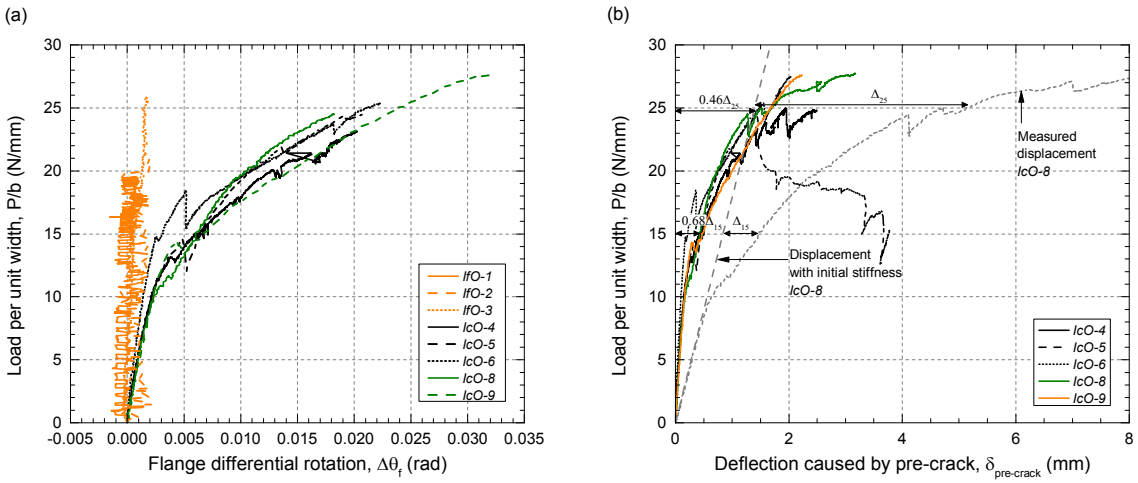

Figure 8: (a) Differential rotation in flange element; (b) contribution of pre-crack to total deflection in *IcO* series.

The effect of the *IcO* specimens' pre-crack (see Figs. 3 (b) and 4 (b)) on their nonlinear behavior was further analyzed. Figure 8 (a) illustrates the differential rotation in the flange, $\Delta\theta_f$, between two sections located 10 mm apart across its thickness. The *IcO* pre-crack was flanked by these two sections. Figure 8 (a) shows that in the *IfO* series, where no pre-crack existed, both sections rotated conjointly ($\Delta\theta_f \approx 0$) while in the *IcO* specimens a non-linear differential rotation, corresponding to the opening of the pre-crack, was registered. The contribution of the pre-crack to the total deflection, $\delta_{pre\text{-}crack}$, was calculated. Figure 8 (b) shows that the *IcO* specimens' stiffness decrease was partially caused by the flange's pre-existing crack – e.g. in *IcO-8*, at 15 / 25-N/mm loads, $\delta_{pre\text{-}crack}$ represented 68 / 46% of the difference between the measured displacement and the expected deflection if the initial stiffness had remained constant up to failure. The pre-crack was thus considered as being the origin of the initial nonlinearity of the *IcO* series, but not of its sustained load-bearing capacity under increasing displacement – the influence of the pre-crack opening reduced with increasing load levels.

Failure occurred due to transverse (through-thickness) tension in the upper (tensioned) fillet, where the first cracks were noticed in both series. However, and regardless of their similar fiber architecture, the *IfO* / *IcO* specimens displayed different crack formation sequences and peak loads. This was ascribed to the fiber arrangement in the web element and in the WFJ itself. In the studied configuration, the load was mainly borne by the triaxial multi-ply fabrics. The triaxial fabrics were evenly distributed across the thickness of the *IcO* specimens' webs, whereas in the *IfO* specimens and close to the WFJ, they were concentrated towards their lower (compressed) side, see Fig. 4. The neutral axis of the web was therefore located closer to its lower face in *IfO* than in *IcO*. Hence, at a same load value (thus equal bending moment), the tension stress in the upper fabrics, and therefore the transverse tension stress in the fillet, was higher in *IfO* than in *IcO*. The first cracking appeared in the *IfO* series close to the surface due to the higher tensile force borne by and higher curvature of the outer fabric, and thus maximum through-thickness stress in that location, see Fig. 7 (a). In the *IcO* specimens, which bore a lower tensile force in the outer fabric, the first cracking (see Fig. 7 (b)) was registered adjacent to the inner fabric next to the roving core, where the maximum curvature, resulting from some apparent wrinkling, was observed (see Fig. 4 (b)). Moreover, this area could be influenced by the proximity of the pre-crack and show lower strength.

The different crack sequences observed in the *IfO*/*IcO* series resulted in different load capacities and failure modes in the two series: the *IfO* specimens exhibited ca. 22% lower peak loads per unit width than the *IcO* specimens and sudden failure, whereas in the *IcO* series failure was preceded by a large displacement development. Additionally, a resin-rich area in the compressed fillet of the *IfO* WFJs (see Fig. 4 (a)) might have also contributed to their lower strength compared to the *IcO* WFJs. Owing to the appearance of the first crack, the delaminated outer thin fabric layer in the *IfO* series no longer contributed to the section's bending stiffness. The bending stiffness reduction, considering the uneven fabric distribution shown in Fig. 4 (a), was however significant (ca. 50%) in the web element and close

to the WFJ. As a result, a sharp load drop was registered at the peak load displacement. Further crack development occurred in the post-peak phase with almost sustained but lower load capacity, see Fig. 6 (a). In the *IcO* specimens, the first cracking resulted in a stiffness decrease, as shown in Fig. 6 (b). The triaxial fabrics above the first crack remained active, enabling the WFJs to bear an increasing load. Subsequently, cracking occurred in the same locations as those registered for the cracks in the *IfO* specimens, although at higher deflections. The upper fabrics were straightened and acted as tensioned ties, which allowed the peak load to be sustained at an approximately constant level. Further crack propagation, resulting in a similar crack pattern to that observed in the *IfO* series (see Fig. 7), led to the progressive inactivation of the upper fabrics and resulted in a lower post-peak capacity comparable to that of the *IfO* specimens, see Fig. 6.

5.2 Energy dissipation capacity of *IcO* series

The *IcO* specimens exhibited nonlinear behavior and development of large deflections towards failure with sustained load-bearing capacity (see Sections 4.2 and 5.1). In addition, the unloading-reloading cycles conducted revealed that the *IcO* series response was not elastic and that inelastic, irrecoverable deflections took place; its behavior could therefore be described as ductile. The capability of the *IcO* WFJs to dissipate energy under local bending, for a monotonic loading case and taking into consideration their viscoelastic behavior, is analyzed to assess their ductility.

Figure 1 (b) can serve to schematically illustrate the energy dissipation behavior of the WFJs under monotonic loading. The envelopes of the experimental load-deflection relationships from Fig. 6 (b) were assumed to be representative of the monotonic behavior and were thus considered to obtain the total energy provided to the WFJs, W_t, up to the considered displacement δ_{max}. The unloading paths were used to obtain the dissipated energy, W_d (W_d equals the area enclosed by the loading and unloading paths). The calculated W_t and W_d per unit width are represented in Fig. 9 (a). The W_t/b and W_d/b values, in J/mm, can be approximated as a function of δ_{max} (mm) by power functions as follows:

$$\frac{W_i}{b}(\delta_{\max}) = a_i \cdot \delta_{\max}{}^{c_i} \tag{5}$$

where $i = t$ (total energy) or d (dissipated energy) and a_i and c_i are calibration parameters fitted to the experimental results (c_i = 1.285 / 1.405 and a_i = 0.0108 / 0.0047 J/mm$^{(1+c)}$ for $i = t$ / d, respectively). The obtained c values indicated that W_t/b and W_d/b augmented with increasing cycle displacement (c>0) at an increasing rate (c>1), showing that for the same displacement increment more work has to be performed and more energy is dissipated at higher than at lower deflection levels. Figure 9 (a) shows that good agreement existed between the experimental results and the power empirical model from Eq. (5) and indicates that the elastic energy W_e per unit width increased with increasing cycle displacement. The augmentation of W_e/b was related to the decrease of stiffness throughout the cycles.

The ratio of the hysteretic energy to the total dissipated energy up to the relevant cycle, $W_{d,hyst}$ / W_d, is given in Fig. 9 (b) throughout the conducted cycles. Figure 9 (b) shows that the energy dissipation due to the viscoelastic behavior (related to $W_{d,hyst}$) was below 40% of the total dissipated energy at early displacement stages and that this ratio decreased rapidly with increasing maximum cycle displacement down to ca. 15% at failure. This showed that damage and the associated crack development represented the main dissipation mechanism of the WFJs, whereas the amount of energy dissipated through viscoelasticity was low except for small displacements, when cracking was still incipient.

The ductility index for the *IcO* WFJs throughout loading ($0 \leq \delta_{max} \leq 20$ mm) was calculated using the energy values per unit width and hence substituting Eq. (5) into Eq. (3) as follows:

$$\mu = \frac{a_d}{a_t} \cdot \delta_{max}{}^{c_d - c_t} \tag{6}$$

where d and t subscripts denote the dissipated and total energy, respectively. The model from Eq. (6) is represented in Fig. 10. A good agreement with the experimental results was observed – they were comprised within ±5% of the modeled values. The modeled ductility index increases with increasing maximum displacement, although at a decreasing rate ($0 < (c_d - c_t) < 1$). As a result, the predicted

ductility index for specimens failing at a 10-mm displacement (e.g. *IcO-6*) represented ca. 91% of the predicted value for those failing at 20 mm (e.g. *IcO-8*) – ductility indices of 0.57 and 0.62 corresponded to 10- and 20-mm δ_{max}, respectively. This suggests that the ratio between the dissipated and total energies – and therefore the ratio between any two of the dissipated, elastic and total energies – did not significantly vary after a certain displacement was attained (9% increase for W_d/W_t from 10- to 20-mm δ_{max} at an approximately constant rate of 0.049/mm).

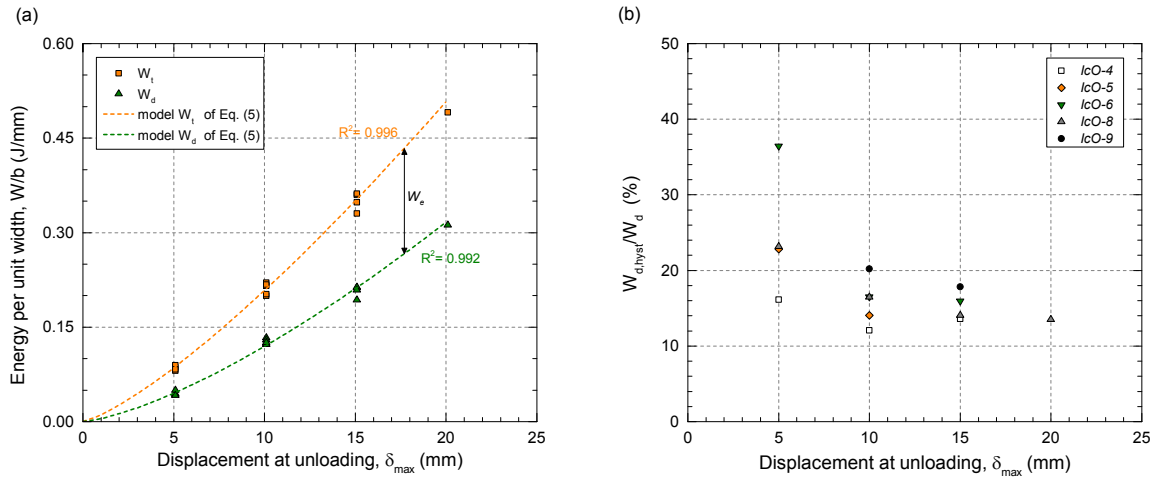

Figure 9: (a) Total and dissipated energies per unit width during monotonic loading; (b) ratio of hysteretic to total dissipated energy throughout cycles.

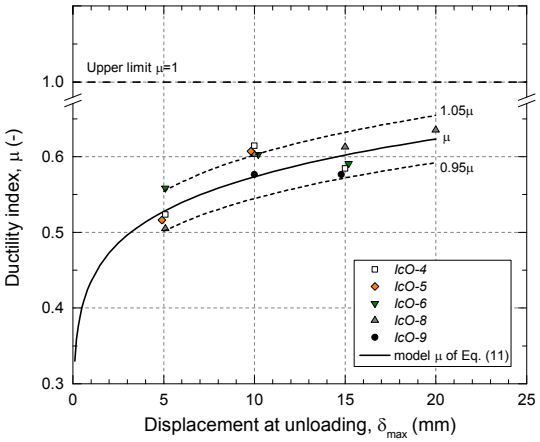

Figure 10: Ductility index for *IcO* WFJs throughout displacement. $\mu = 1$ indicates rigid-plastic behavior.

6 CONCLUSIONS

The behavior under local bending of two types of web-flange junctions (WFJs) from the *DS* deck (*IfO* and *IcO* series) and the energy dissipation capacity, under monotonic loading, of one of them showing progressive failure (*IcO*) were experimentally studied. The following conclusions were drawn:

- Despite their similar geometry and fiber architecture, the behavior under local bending differed in the *IfO* and *IcO* series owing to dissimilar initial imperfections. The *IfO* specimens showed linear behavior up to failure, which occurred abruptly. The *IcO* specimens exhibited markedly nonlinear behavior, partially caused by a pre-existing crack in the flange element, and progressive failure.
- The WFJs failed due to transverse (through-thickness) tension in their tensioned fillet. The *IfO* specimens showed a 22% lower peak load than the *IcO* specimens due to a less even distribution of the load-bearing fabrics across the web element thickness.

- A power model was developed for modeling the total and dissipated energies of the *IcO* WFJs under monotonic loading. Higher rates at higher displacement levels were obtained for both the total and dissipated energies.
- The *IcO* WFJs dissipated at failure up to 62% of the total energy provided. The ductility index, defined as the ratio of the dissipated to the total energy, did not significantly increase as from a 10-mm displacement.
- The main energy dissipation mechanism of the *IcO* WFJs was related to the crack development. Given the viscoelastic nature of FRP materials, dissipation through viscoelastic losses did also occur. The viscoelastic contribution to energy dissipation was significant at low deflection levels, when cracking was still incipient; however, it rapidly decreased to ca. 15% with increasing displacement and progression of cracking.

Further research is required to evaluate the influence of the viscoelastic character of the FRP material on the energy dissipation capability of the WFJs when subjected to cyclic loading. Under cyclic loading up to a previously established load/displacement level, dissipation through viscosity-related losses can occur without any damage increase; thus, the energy dissipation owing to the material viscoelasticity may be better exploited.

REFERENCES

[1] T. Keller and J. de Castro, System ductility and redundancy of FRP beam structures with ductile adhesive joints, *Composites Part B: Engineering,* **36**, 2005, pp. 586-596 (doi: 10.1016/j.compositesb.2005.05.001).

[2] L.C. Bank, Progressive failure and ductility of FRP composites for construction: review, *Journal of Composites for Construction,* **17**, 2013, pp. 406-419 (doi: 10.1061/(ASCE)CC.1943-5614.0000355).

[3] G.M. Van Erp, Robustness of fibre composite structures loaded in flexure, *FRP Composites in Civil Engineering, Proceedings of International Conference on FRP Composites in Civil Engineering 2001 (Ed. J.G. Teng), Hong Kong, China, December 12-15, 2001,* Elsevier, Oxford, 2001, pp. 1421-1426.

[4] T. Keller and H. Gürtler, In-plane compression and shear performance of FRP bridge decks acting as top chord of bridge girders, *Composites Structures,* **72**, 2006, pp. 151-162 (doi: 10.1016/j.compstruct.2004.11.004).

[5] S. Yanes, J. de Castro, A.P. Vassilopoulos and T. Keller, Static performance in transverse direction of pultruded GFRP bridge decks, *Proceedings of 7th International Conference on FRP Composites in Civil Engineering 2014 (Ed. R. El-Hacha), Vancouver, Canada, August 20-22, 2014,* International Institute for FRP in Construction, Paper 138, 2014.

[6] I. Widyatmoko, C. Ellis and J.M. Read, Energy dissipation and the deformation resistance of bituminous mixtures, *Materials and Structures,* **32**, 1999, pp. 218-223 (doi: 10.1007/BF02481518).

[7] N.F. Grace, A. Soliman, G. Abdel-Sayed and K. Saleh, Behavior and ductility of simple and continuous FRP reinforced beams, *Journal of Composites for Construction,* **2**, 1998, pp. 186-194 (doi: 10.1061/(ASCE)1090-0268(1998)2:4(186)).